PHILOSOPHICAL TRANSACTIONS OF THE ROYAL SOCIETY A MATHEMATICAL, PHYSICAL & ENGINEERING SCIENCES

High–rate material modelling and validation using the Taylor cylinder impact test

P. J. Maudlin, G. T. Gray III, C. M. Cady and G. C. Kaschner

Phil. Trans. R. Soc. Lond. A 1999 **357**, 1707-1729
doi: 10.1098/rsta.1999.0397

THE ROYAL SOCIETY

High-rate material modelling and validation using the Taylor cylinder impact test

By P. J. Maudlin, G. T. Gray III, C. M. Cady and G. C. Kaschner

PO Box 1663, Los Alamos National Laboratory, Los Alamos, NM 87545, USA

Taylor cylinder impact testing is used to validate anisotropic elastoplastic constitutive modelling by comparing polycrystal-computed yield-surface shapes (topography) with measured shapes from post-test Taylor specimens and quasi-static compression specimens. Measured yield-surface shapes are extracted from the experimental post-test geometries using classical r-value definitions modified for arbitrary stress state and specimen orientation. Rolled tantalum (body-centred-cubic metal) plate and clock-rolled zirconium (hexagonal-close-packed metal) plate are both investigated. The results indicate that an assumption of topography invariance with respect to strain rate is well justified for tantalum. However, a strong sensitivity of topography with respect to strain rate for zirconium was observed, implying that some accounting for a deformation mechanism rate dependence associated with lower-symmetry materials should be included in the constitutive modelling. Discussion of the importance of this rate dependence and texture evolution in formulating constitutive models appropriate for finite-element model applications is provided.

Keywords: anisotropic plasticity; polycrystal plasticity; Taylor anvil tests; tantalum deformation; zirconium deformation; rate-dependent plasticity

1. Introduction

The importance of an accurate constitutive description for large deformation involving anisotropic metallic materials has been demonstrated in many applications; the earring of deep-drawn cups is a classic low-strain-rate example. Our interest is to develop more accurate descriptions of material strength for high-rate forming applications, and to integrate such descriptions into the appropriate continuum mechanics codes. Over the last decade, the computing power (i.e. memory, processor speed and number of processors) available for numerical analysis has increased substantially. As a result, the computational tools available for simulating high deformation processes have recently improved to accommodate more complex descriptions of material behaviour. However, even with state-of-the-art computing power, there is still a need to be aware of the cost of using advanced material modelling in the codes and balancing this cost with the *realized* accuracy improvement in predictive capability.

Our Hookean modelling combines an appropriate elastic stiffness, a physically based flow stress model describing rate and thermally dependent hardening, and a yield-surface representation, again physically based on experimental measurements of the crystallographic texture and polycrystal simulations. This elastoplastic property information is used in classical associative flow constitutive formulations using unrotated (material frame) tensors, with emphasis on cubic and hexagonal materials.

This approach bridges the gap between single crystal and application length-scales with continuum constructs in order to address high-rate deformation processes with more physical fidelity.

Taylor cylinder impact testing (Taylor 1948; Lee & Tupper 1954; Hawkyard 1969; Wilson *et al*. 1989; Maudlin *et al*. 1997, 1999) has been used to validate constitutive modelling in the presence of gradients of stress, strain and strain rate that this integrated test affords. For example, an investigation of plastic wave propagation in a Taylor test comparing time-resolved experimental data using high-speed photography with two-dimensional dynamic simulations is given by Maudlin *et al*. (1997). The work of Maudlin *et al*. (1999) presents a static comparison of calculated three-dimensional final shapes with measured shapes of post-test specimens for an orthotropic material. In this effort, r-values (straining ratios) are extracted from quasi-static compression data and high-rate Taylor impact specimens, and compared to polycrystal simulations using *yield-surface shape* as the basis for comparison. Using this approach, inferences can be made as to the evolution and rate dependence of yield-surface shape (topography) for a given material. Results from such comparisons are presented here. Examples and counter-examples of the importance of yield-surface topography and the effect of texture evolution on topography are discussed.

2. Theory

Constitutive modelling appropriate for anisotropic elastic-plastic flow of metal is first reviewed, followed by an extension of the classic definition of r-value (Hill 1950) to accommodate *arbitrary* stress state and material orientation. The relationship between r-value and yield-surface shape is then developed as a basis for comparison with experimental data.

(*a*) *Elastoplastic constitutive modelling*

We begin with a continuum level constitutive description that uses the rate form of Hooke's law, i.e. hypoelasticity, which is a very good approximation for metals that exhibit small elastic strains:

$$\underline{\underline{\dot{\sigma}}} = \underline{\underline{\underline{\underline{E}}}} : \underline{\underline{D}}^{\mathrm{e}}. \tag{2.1}$$

This relationship assumes the unrotated Cauchy stress $\underline{\underline{\sigma}}$ as a stress measure, and the unrotated rate-of-deformation tensor $\underline{\underline{D}}$ (symmetric part of the velocity gradient tensor) as an appropriate work conjugate rate-of-strain measure. Tensor *order* is denoted here by the number of underbars. The quantity $\underline{\underline{D}}^{\mathrm{e}}$ is the elastic part of $\underline{\underline{D}}$ that follows from a partition assumption for the elastic and plastic rates of strain, i.e.

$$\underline{\underline{D}} = \underline{\underline{D}}^{\mathrm{e}} + \underline{\underline{D}}^{\mathrm{p}}. \tag{2.2}$$

Deviatoric versions of equations (2.1) and (2.2), which are more convenient for incompressible materials, can be derived as:

$$\underline{\underline{\dot{s}}} = \underline{\underline{\underline{\underline{\xi}}}} : \underline{\underline{d}}^{\mathrm{e}} \tag{2.3}$$

and

$$\underline{\underline{d}} = \underline{\underline{d}}^{\mathrm{e}} + \underline{\underline{d}}^{\mathrm{p}}, \tag{2.4}$$

where

$$\underline{\underline{\underline{\underline{\xi}}}}$$

is the deviator of the fourth-order elastic stiffness tensor

$$\underline{\underline{\underline{\underline{E}}}}.$$

Next, consider the classical associated flow rule for evolving the plastic rate-of-strain $\underline{\underline{d}}^{\mathrm{p}}$:

$$\underline{\underline{d}}^{\mathrm{p}} = \dot{\lambda}\frac{\partial f}{\partial \underline{\underline{s}}}, \tag{2.5}$$

where the quantity $\dot{\lambda}$ is a time-dependent scalar, and the quantity f is a continuous yield function known from either polycrystal predictions (Maudlin & Schiferl 1996; Maudlin *et al*. 1996) or experimental interrogation (Hill 1950). This function f is five dimensional in terms of independent deviatoric stress components $(s_{11}, s_{22}, s_{23}, s_{31}, s_{12})$, and physically constrains the magnitude of $\underline{\underline{s}}$ during plastic flow. Its stress gradient determines the direction of the plastic rate-of-strain tensor $\underline{\underline{d}}^{\mathrm{p}}$, as indicated in equation (2.5). A general quadratic form for f can be written as

$$f \equiv \tfrac{1}{2}\underline{\underline{s}} : \underline{\underline{\underline{\underline{\alpha}}}} : \underline{\underline{s}} - \sigma^2 = 0, \tag{2.6}$$

where

$$\underline{\underline{\underline{\underline{\alpha}}}}$$

is a fourth-order major and minor symmetric shape tensor, and σ is a flow stress scalar assumed to be a function of strain, strain rate and temperature invariants.

The flow stress σ model of choice for our dynamic applications (see Maudlin *et al*. 1995, 1997, 1999) is the so-called mechanical threshold stress (MTS) model (Follansbee & Kocks 1988). Briefly, the model represents a superposition of contributions to the flow stress where each contribution is a mobile dislocation interaction with some barrier:

$$\sigma = \sigma_{\mathrm{a}} + \frac{\mu}{\mu_0}\sum_i s_{\mathrm{th},i}\hat{\sigma}_{\mathrm{i}}. \tag{2.7}$$

The product under the summation sign in equation (2.7) contains the internal variable $\hat{\sigma}$, called the mechanical threshold stress (related to the forest dislocation density), which is multiplied by a thermal activation function s_{th}. The athermal stress σ_{a} represents dislocation interactions with long-range barriers such as grain boundaries, and is typically assumed to be constant although it is formally dependent on grain size.

The most important evolution equation for $\hat{\sigma}$ is a differential hardening law for the build-up of forest dislocations:

$$\frac{\partial \hat{\sigma}}{\partial \varepsilon^{\mathrm{p}}} = \Theta_0\left[1 - F\left(\frac{\hat{\sigma}}{\hat{\sigma}_{\mathrm{s}}}\right)\right]. \tag{2.8}$$

In this equation, Θ_0 represents hardening due to dislocation generation, and the product $\Theta_0 \cdot F$ represents softening due to recovery. The threshold stress at zero strain hardening $\hat{\sigma}_{\mathrm{s}}$ is called the saturation threshold stress. Relationships for F, Θ, $\hat{\sigma}_{\mathrm{s}}$ are, typically, material specific, and formally depend on temperature T and plastic strain rate $\dot{\varepsilon}^{\mathrm{p}}$. The choice of $\hat{\sigma}/\hat{\sigma}_{\mathrm{s}}$ for the function F gives a Voce form for the hardening law of equation (2.8).

For thermal-activation controlled deformation, the function s_{th} in equation (2.7) has an Arrhenius form:

$$s_{\mathrm{th},i} = \left[1 - \left(\frac{kT\ln(\dot{\varepsilon}_{0i}/\dot{\varepsilon}^{\mathrm{p}})}{\mu b^3 g_{0i}}\right)^{1/q_i}\right]^{1/p_i}, \tag{2.9}$$

where the exponents p and q are material constants, $\dot{\varepsilon}_0$ is a reference strain rate, μ is a temperature-dependent shear modulus, k is Boltzmann's constant, b is the magnitude of Burger's vector and g_0 is a normalized activation energy for a given dislocation/obstacle interaction. The reader is referred to Follansbee & Kocks (1988) and Chen & Gray (1996) for more detail concerning the development and interpretation of equations (2.7)–(2.9).

Returning now to the yield function given by equation (2.6), note that for orthotropic materials (mirror plane symmetry where the deviator tensor

$$\underline{\underline{\underline{\alpha}}}$$

has six independent constants), equation (2.6) simplifies to the quadratic function (Hill 1950),

$$f \equiv \tfrac{1}{2}[(G+H)s_{11}^2 + (F+H)s_{22}^2 + (F+G)s_{33}^2 - 2Hs_{11}s_{22} - 2Gs_{11}s_{33} - 2Fs_{22}s_{33} + 2Ls_{23}^2 + 2Ms_{31}^2 + 2Ns_{12}^2] - \sigma^2 = 0, \tag{2.10}$$

and the shape tensor

$$\underline{\underline{\underline{\alpha}}},$$

written in Voigt–Mandel components, can be expressed in terms of the Hill coefficients of equation (2.10):

$$VM(\underline{\underline{\underline{\alpha}}})_{\mathrm{Hill48}} = \begin{pmatrix} G+H & -H & -G & 0 & 0 & 0 \\ -H & F+H & -F & 0 & 0 & 0 \\ -G & -F & F+G & 0 & 0 & 0 \\ 0 & 0 & 0 & L & 0 & 0 \\ 0 & 0 & 0 & 0 & M & 0 \\ 0 & 0 & 0 & 0 & 0 & N \end{pmatrix}. \tag{2.11}$$

A von Mises yield function can be recovered from equation (2.6) using the following second-order tensor for $\underline{\underline{\underline{\alpha}}}$:

$$VM(\underline{\underline{\underline{\alpha}}})_{\text{von Mises}} = \begin{pmatrix} 2 & -1 & -1 & 0 & 0 & 0 \\ -1 & 2 & -1 & 0 & 0 & 0 \\ -1 & -1 & 2 & 0 & 0 & 0 \\ 0 & 0 & 0 & 3 & 0 & 0 \\ 0 & 0 & 0 & 0 & 3 & 0 \\ 0 & 0 & 0 & 0 & 0 & 3 \end{pmatrix}. \tag{2.12}$$

To achieve a final constitutive relationship in rate form (useful for explicit continuum code computations), we substitute equations (2.4), (2.5) and (2.6) back into equation (2.3), giving the unrotated stress rate applied numerically in other efforts (see Maudlin *et al*. 1995, 1999):

$$\dot{\underline{\underline{s}}} = \underline{\underline{\underline{\underline{\xi}}}} : (\underline{\underline{d}} - \dot{\lambda}\underline{\underline{\underline{\underline{\alpha}}}} : \underline{\underline{s}}). \tag{2.13}$$

(*b*) *Classical and generalized r-values*

Following the classic work of Hill (1950), we define an r-value (r) as a ratio of orthogonal plastic strain rates realized in a metal specimen of rectangular cross-section loaded in a state of uniaxial stress (tension or compression). These straining rates are logically in directions perpendicular to the direction of loading and the free surfaces. For example, if '1' is the direction of uniaxial loading, it follows from the boundary conditions that $s_{11} = -2s_{22} = -2s_{33} = \frac{2}{3}\sigma$ in the laboratory test frame, and the corresponding instantaneous r-value definition is

$$r_1 \equiv \frac{\underline{e}_2 \cdot \underline{\underline{d}}^{\mathrm{p}} \cdot \underline{e}_2}{\underline{e}_3 \cdot \underline{\underline{d}}^{\mathrm{p}} \cdot \underline{e}_3}. \tag{2.14\,a}$$

Here, the $\underline{e}_i$ are Cartesian base vectors for the laboratory reference frame, and the r-value subscript designates the *loading direction*. Similar r-value definitions for loading in the other two directions, i.e. 2 and 3, respectively, follow as

$$r_2 \equiv \frac{\underline{e}_1 \cdot \underline{\underline{d}}^{\mathrm{p}} \cdot \underline{e}_1}{\underline{e}_3 \cdot \underline{\underline{d}}^{\mathrm{p}} \cdot \underline{e}_3} \quad \text{and} \quad r_3 \equiv \frac{\underline{e}_1 \cdot \underline{\underline{d}}^{\mathrm{p}} \cdot \underline{e}_1}{\underline{e}_2 \cdot \underline{\underline{d}}^{\mathrm{p}} \cdot \underline{e}_2}. \tag{2.14\,b}$$

The definition of r-value can be generalized into matrix form:

$$\underline{\underline{r}} \equiv \begin{pmatrix} 1 & r_{12} & r_{13} \\ r_{21} & 1 & r_{23} \\ r_{31} & r_{32} & 1 \end{pmatrix}, \quad \text{where } r_{IJ} = \frac{\underline{e}_I \cdot \underline{\underline{d}}^{\mathrm{p}} \{\underline{\underline{Q}}^{\mathrm{T}} \cdot \underline{\underline{s}} \cdot \underline{\underline{Q}}\} \cdot \underline{e}_I}{\underline{e}_J \cdot \underline{\underline{d}}^{\mathrm{p}} \{\underline{\underline{Q}}^{\mathrm{T}} \cdot \underline{\underline{s}} \cdot \underline{\underline{Q}}\} \cdot \underline{e}_J}, \quad \text{no sum } I, J, \tag{2.15}$$

where the tensor, $\underline{\underline{Q}}$, is a proper orthogonal rotation that properly aligns the direction of loading for each value of r_{IJ}:

$$\underline{\underline{Q}} = \varepsilon_{IJK}\underline{\underline{Q}}_K, \quad \text{where } \underline{\underline{Q}}_1 = \underline{\underline{I}}, \quad \underline{\underline{Q}}_2 = -\begin{pmatrix} 0 & -1 & 0 \\ 1 & 0 & 0 \\ 0 & 0 & 1 \end{pmatrix}, \quad \underline{\underline{Q}}_3 = \begin{pmatrix} 0 & 0 & -1 \\ 0 & 1 & 0 \\ 1 & 0 & 0 \end{pmatrix}. \tag{2.16}$$

Here, ε_{IJK} is the third-order alternator tensor and, for clarity, the functional dependence of the rate-of-straining tensor $\underline{\underline{d}}^{\mathrm{p}}$ on the rotation $\underline{\underline{Q}}$ is shown explicitly in equation (2.15). Also note that the matrix definition of r-value contains only three independent coefficients: r_{12}, r_{13}, r_{23}; the relationship $r_{IJ} = -1/r_{JI}$ holds between transposed components, and, obviously, $r_{II} = 1$ (no sum on I) from inspection of equation (2.15).

Next, we substitute the associated flow rule given by equation (2.5) into equation (2.15), obtaining an r-value involving only yield-surface stress gradients $\partial f/\partial \underline{\underline{s}}$ after cancellation of $\dot{\lambda}$. Recalling from equation (2.13) the form of $\partial f/\partial \underline{\underline{s}}$ for a

quadratic yield function, and incorporating $\underline{\underline{Q}}$ to impose the direction of loading, gives

$$\frac{\partial f}{\partial \underline{\underline{s}}} = \underline{\underline{\alpha}} : (\underline{\underline{Q}}^{\mathrm{T}} \cdot \underline{\underline{s}} \cdot \underline{\underline{Q}}), \quad \text{or in indicial notation } \frac{\partial f}{\partial s_{ij}} = \alpha_{ijkl} Q^{\mathrm{T}}_{km} s_{mn} Q_{nl}, \tag{2.17}$$

and, after substitution of equation (2.17) back into equation (2.15), we obtain the final r-value result:

$$r_{IJ} = \frac{\underline{e}_I \cdot \underline{\underline{\underline{\alpha}}} : (\underline{\underline{Q}}^{\mathrm{T}} \cdot \underline{\underline{s}} \cdot \underline{\underline{Q}}) \cdot \underline{e}_I}{\underline{e}_J \cdot \underline{\underline{\underline{\alpha}}} : (\underline{\underline{Q}}^{\mathrm{T}} \cdot \underline{\underline{s}} \cdot \underline{\underline{Q}}) \cdot \underline{e}_J} \quad \text{or} \quad r_{IJ} = \frac{\alpha_{IIkl} Q^{\mathrm{T}}_{km} s_{mn} Q_{nl}}{\alpha_{JJpq} Q^{\mathrm{T}}_{pr} s_{rs} Q_{sq}}, \quad \text{no sum } I, J. \tag{2.18}$$

As an example, consider the case of uniaxial stress in the $\underline{e}_1$-direction ($\underline{\underline{Q}}_{K=1}$), where the stress deviator simplifies to

$$\underline{\underline{s}} = s_{11} \begin{pmatrix} 1 & 0 & 0 \\ 0 & -\frac{1}{2} & 0 \\ 0 & 0 & -\frac{1}{2} \end{pmatrix}, \tag{2.19}$$

and the yield gradient given by equation (2.17) becomes

$$\frac{\partial f}{\partial s_{ij}} = s_{11}[\alpha_{ij11} - \tfrac{1}{2}\alpha_{ij22} - \tfrac{1}{2}\alpha_{ij33}]. \tag{2.20}$$

Evaluation of the r-value (specifically r_{23}) follows from equation (2.18) as just a ratio of the normal shape coefficients:

$$r_{23} = \alpha_{1122}/\alpha_{1133}. \tag{2.21}$$

In like manner, uniaxial stress loading in the

$$\underline{e}_2 \quad (\underline{\underline{Q}}_{K=2}) \quad \text{and} \quad \underline{e}_3 \quad (\underline{\underline{Q}}_{K=3})$$

directions results in similar expressions for the other orthogonal r_{IJ}, and, thus, we obtain for the r-value matrix

$$\underline{\underline{r}} = \begin{pmatrix} 1 & \dfrac{\alpha_{1133}}{\alpha_{2233}} & \dfrac{\alpha_{1122}}{\alpha_{2233}} \\ -\dfrac{\alpha_{2233}}{\alpha_{1133}} & 1 & \dfrac{\alpha_{1122}}{\alpha_{1133}} \\ -\dfrac{\alpha_{2233}}{\alpha_{1122}} & -\dfrac{\alpha_{1133}}{\alpha_{1122}} & 1 \end{pmatrix}. \tag{2.22}$$

Expressions for the *normal* shape coefficients (and hence the r_{IJ}) as functions of the deviator stress are next derived by solving a system of six equations for the six unknowns $\alpha_{ijkl}\delta_{kl}\delta_{ij}$, where δ_{ij} is the Kronecker delta function. Three equations are consecutively generated by substituting the condition of uniaxial stress (e.g. equation (2.19)) into the yield function equation (2.6) for each of the three Cartesian directions $\underline{e}_i$. Three additional equations are available given that

$$\underline{\underline{\underline{\alpha}}}$$

is a deviator tensor and the six coefficients $\alpha_{ijkl}\delta_{kl}\delta_{ij}$ are dependent, i.e. each row (or column) of the upper 3×3 sub-matrix of

$$VM(\underline{\underline{\underline{\alpha}}})$$

sums to zero:

$$\alpha_{11ii} = 0, \tag{2.23 a}$$

$$\alpha_{22ii} = 0, \tag{2.23 b}$$

$$\alpha_{33ii} = 0. \tag{2.23 c}$$

Solving this 6×6 system of equations for $\alpha_{ijkl}\delta_{kl}\delta_{ij}$ produces the solution:

$$\alpha_{1111} = \frac{8\sigma^2}{9s_{11}^2}, \tag{2.24 a}$$

$$\alpha_{2222} = \frac{8\sigma^2}{9s_{22}^2}, \tag{2.24 b}$$

$$\alpha_{3333} = \frac{8\sigma^2}{9s_{33}^2}, \tag{2.24 c}$$

$$\alpha_{2233} = \tfrac{4}{9}\sigma^2\left(\frac{1}{s_{11}^2} - \frac{1}{s_{33}^2} - \frac{1}{s_{22}^2}\right), \tag{2.24 d}$$

$$\alpha_{1133} = \tfrac{4}{9}\sigma^2\left(\frac{1}{s_{22}^2} - \frac{1}{s_{11}^2} - \frac{1}{s_{33}^2}\right), \tag{2.24 e}$$

$$\alpha_{1122} = \tfrac{4}{9}\sigma^2\left(\frac{1}{s_{33}^2} - \frac{1}{s_{11}^2} - \frac{1}{s_{22}^2}\right). \tag{2.24 f}$$

The deviatoric stress components (s_{11}, s_{22}, s_{33}) in equations (2.24) are uniaxial values as measured in three independent orthogonal tests. These relationships assume that the flow stress σ is a known function characterized from uniaxial stress data in a specific $\underline{e}_i$ direction.

Recalling the relationship between the components of

$$\underline{\underline{\underline{\underline{\alpha}}}}$$

and F, G and H as given by equation (2.11), a similar set of equations for F, G and H as a function of deviatoric stress can be obtained by inspection of equations (2.24):

$$F = \tfrac{4}{9}\sigma^2\left(\frac{1}{s_{22}^2} + \frac{1}{s_{33}^2} - \frac{1}{s_{11}^2}\right), \tag{2.25 a}$$

$$G = \tfrac{4}{9}\sigma^2\left(\frac{1}{s_{33}^2} + \frac{1}{s_{11}^2} - \frac{1}{s_{22}^2}\right), \tag{2.25 b}$$

$$H = \tfrac{4}{9}\sigma^2\left(\frac{1}{s_{11}^2} + \frac{1}{s_{22}^2} - \frac{1}{s_{33}^2}\right). \tag{2.25 c}$$

The above formulations assume that the material reference frame (where f is characterized) and the laboratory test frame are coincident. However, if the two frames differ by some three-dimensional rigid body rotation, then the derivation for the r-values is somewhat more complicated. Physically, this situation would arise when the material frame (which is usually based on the microstructural symmetry of the material) differs in orientation from the laboratory test frame, where some geometrical specimen is loaded. An example of this situation is given below. For clarity in the

subsequent discussion, we associate the Cartesian base vectors $\bar{\underline{e}}_i$ with the material frame and, as used above, the Cartesian base vectors $\underline{e}_i$ with the laboratory frame.

In order to derive a more general r-value definition, recall that the yield function f as given by equation (2.6) is a function of deviatoric stress, as observed with respect to the material frame. It therefore depends on the unrotated stress state $\bar{\underline{\underline{s}}}$ (the overbar designates *unrotated material frame* tensors). This unrotated stress differs from the laboratory stress $\underline{\underline{s}}$ by a rigid body rotation represented by the proper orthogonal tensor $\underline{\underline{R}}$ ($\underline{e}_i = \underline{\underline{R}} \cdot \bar{\underline{e}}_i$):

$$\bar{\underline{\underline{s}}} = \underline{\underline{R}}^{\mathrm{T}} \cdot \underline{\underline{s}} \cdot \underline{\underline{R}}, \quad \text{or in indicial notation } \bar{s}_{ij} = R^{\mathrm{T}}_{ik} s_{kl} R_{lj}. \tag{2.26}$$

Noting the r-value relationship given by equation (2.15), the stress gradient given by equation (2.5) is expanded using the chain rule such that

$$\frac{\partial f}{\partial \underline{\underline{s}}} = \frac{\partial f}{\partial \bar{\underline{\underline{s}}}} : \frac{\partial \bar{\underline{\underline{s}}}}{\partial \underline{\underline{s}}} \quad \text{or} \quad \frac{\partial f}{\partial s_{ij}} = \frac{\partial f}{\partial \bar{s}_{kl}} \frac{\partial \bar{s}_{kl}}{\partial s_{ij}}, \tag{2.27}$$

and the stress derivative $\partial \bar{\underline{\underline{s}}} / \partial \underline{\underline{s}}$ follows from equation (2.26) as

$$\frac{\partial \bar{\underline{\underline{s}}}}{\partial \underline{\underline{s}}} = \underline{\underline{R}}^{\mathrm{T}} \cdot \frac{\partial \underline{\underline{s}}}{\partial \underline{\underline{s}}} \cdot \underline{\underline{R}} = \underline{\underline{R}}^{\mathrm{T}} \cdot \underline{\underline{\underline{\underline{\delta}}}} \cdot \underline{\underline{R}}$$

$$\text{or} \quad \frac{\partial \bar{s}_{kl}}{\partial s_{ij}} = R^{\mathrm{T}}_{km} \frac{\partial s_{mn}}{\partial s_{ij}} R_{nl} = R^{\mathrm{T}}_{km} \delta_{mi} \delta_{jn} R_{nl} = R^{\mathrm{T}}_{ki} R_{jl}. \tag{2.28}$$

The tensor

$$\underline{\underline{\underline{\underline{\delta}}}}$$

is the fourth-order identity tensor ($\delta_{ijkl} = \delta_{ik}\delta_{jl}$). Substitution of equations (2.5), (2.27) and (2.28) into the r-value expression given by equation (2.15) results in the relationship

$$r_{IJ} = \frac{\underline{e}_I \cdot \left\{ \dfrac{\partial f}{\partial \bar{\underline{\underline{s}}}} : (\underline{\underline{R}}^{\mathrm{T}} \cdot \underline{\underline{\underline{\underline{\delta}}}} \cdot \underline{\underline{R}}) \right\} \cdot \underline{e}_I}{\underline{e}_J \cdot \left\{ \dfrac{\partial f}{\partial \bar{\underline{\underline{s}}}} : (\underline{\underline{R}}^{\mathrm{T}} \cdot \underline{\underline{\underline{\underline{\delta}}}} \cdot \underline{\underline{R}}) \right\} \cdot \underline{e}_J} \quad \text{or} \quad r_{IJ} = \frac{\dfrac{\partial f}{\partial \bar{s}_{kl}} R^{\mathrm{T}}_{kI} R_{Il}}{\dfrac{\partial f}{\partial \bar{s}_{rs}} R^{\mathrm{T}}_{rJ} R_{Js}}, \quad \text{no sum } I, J. \tag{2.29}$$

In this general form, the r-value can accommodate an arbitrary (but continuous) yield function. If the quadratic form of equation (2.6) is assumed for f, then equation (2.29) specifies to

$$r_{IJ} = \frac{\underline{e}_I \cdot \{[\underline{\underline{\underline{\underline{\alpha}}}} : \bar{\underline{\underline{s}}}] : [\underline{\underline{R}}^{\mathrm{T}} \cdot \underline{\underline{\underline{\underline{\delta}}}} \cdot \underline{\underline{R}}]\} \cdot \underline{e}_I}{\underline{e}_J \cdot \{[\underline{\underline{\underline{\underline{\alpha}}}} : \bar{\underline{\underline{s}}}] : [\underline{\underline{R}}^{\mathrm{T}} \cdot \underline{\underline{\underline{\underline{\delta}}}} \cdot \underline{\underline{R}}]\} \cdot \underline{e}_J}, \quad \text{no sum } I, J, \tag{2.30 a}$$

or

$$r_{IJ} = \frac{\alpha_{ijkl} \bar{s}_{kl} R_{Ij}}{\alpha_{rsuv} \bar{s}_{uv} R_{Js}}, \quad \text{no sum } I, J. \tag{2.30 b}$$

If the unrotated stress is replaced with the laboratory stress via equation (2.26), we obtain the more useful, albeit more complicated, laboratory form

$$r_{IJ} = \frac{\underline{e}_I \cdot \{[\underline{\underline{\underline{\underline{\alpha}}}} : (\underline{\underline{R}}^{\mathrm{T}} \cdot \underline{\underline{Q}}^{\mathrm{T}} \cdot \underline{\underline{s}} \cdot \underline{\underline{Q}} \cdot \underline{\underline{R}})] : [\underline{\underline{R}}^{\mathrm{T}} \cdot \underline{\underline{\underline{\underline{\delta}}}} \cdot \underline{\underline{R}}]\} \cdot \underline{e}_I}{\underline{e}_J \cdot \{[\underline{\underline{\underline{\underline{\alpha}}}} : (\underline{\underline{R}}^{\mathrm{T}} \cdot \underline{\underline{Q}}^{\mathrm{T}} \cdot \underline{\underline{s}} \cdot \underline{\underline{Q}} \cdot \underline{\underline{R}})] : [\underline{\underline{R}}^{\mathrm{T}} \cdot \underline{\underline{\underline{\underline{\delta}}}} \cdot \underline{\underline{R}}]\} \cdot \underline{e}_J}, \quad \text{no sum } I, J, \tag{2.31 a}$$

or

$$r_{IJ} = \frac{\alpha_{ijkl} R^{\mathrm{T}}_{km} Q^{\mathrm{T}}_{mp} s_{pq} Q_{qn} R_{nl} R^{\mathrm{T}}_{iI} R_{Ij}}{\alpha_{rsuv} R^{\mathrm{T}}_{uw} Q^{\mathrm{T}}_{wy} s_{yz} Q_{zx} R_{xv} R^{\mathrm{T}}_{rJ} R_{Js}}, \quad \text{no sum } I, J. \tag{2.31 b}$$

Equations (2.31) represent general r-value expressions for an *arbitrary stress state* and for *an arbitrary orientation difference* between the material and laboratory reference frames. Therefore, stress states other than uniaxial stress can be accommodated, and $\underline{r}$ still retains its basic definition as a ratio of normal straining rates realized in two orthogonal directions. Note that for an arbitrary orientation difference between the material and laboratory frames, $\underline{\underline{R}}$ assumes the three-dimensional form

$$\underline{\underline{R}} = \begin{pmatrix} \cos\phi & -\sin\phi & 0 \\ \sin\phi & \cos\phi & 0 \\ 0 & 0 & 1 \end{pmatrix} \begin{pmatrix} 1 & 0 & 0 \\ 0 & \cos\theta & -\sin\theta \\ 0 & \sin\theta & \cos\theta \end{pmatrix} \begin{pmatrix} \cos\psi & -\sin\psi & 0 \\ \sin\psi & \cos\psi & 0 \\ 0 & 0 & 1 \end{pmatrix}. \tag{2.32}$$

Here, the Euler angles ψ, θ, ϕ represent right-hand-rule plane rotations, as per the convention described by Noble (1969).

As an example of equations (2.31), assume plane rotation around the 3-axis such that $\underline{\underline{R}}$ becomes

$$\underline{\underline{R}} = \begin{pmatrix} \cos\psi & -\sin\psi & 0 \\ \sin\psi & \cos\psi & 0 \\ 0 & 0 & 1 \end{pmatrix}, \tag{2.33}$$

and the laboratory observed stress is again uniaxial in the 1-direction as given by equation (2.16), i.e.

$$\underline{\underline{Q}} = \underline{\underline{I}}.$$

Expanding the summations of equation (2.31 *b*), substituting in equations (2.16) and (2.33), and noting the deviator relationships given by equations (2.20) gives

$$r_{23} = \frac{\alpha_{1122} + (\alpha_{1111} + \alpha_{2222} - 2\alpha_{1122} - 4\alpha_{1212}) \sin^2\psi \cos^2\psi}{\alpha_{2233} \sin^2\psi + \alpha_{1133} \cos^2\psi}. \tag{2.34}$$

Replacing the tensor components α_{ijkl} in equation (2.34) with Hill coefficients from equation (2.8) gives the classic result (Hill 1950) for an r-value specimen cut from sheet metal at an arbitrary orientation ψ with respect to the rolling direction:

$$r_{23} = \frac{H + (2N - F - G - 4H) \sin^2\psi \cos^2\psi}{F \sin^2\psi + G \cos^2\psi}. \tag{2.35}$$

3. Low-rate yield-surface comparisons

Experimental data-sets are presented for both tantalum and zirconium metals: stress–strain loading curves were measured for compression specimens subjected to a state of uniaxial stress. This information is converted into yield-surface shape coefficients that are subsequently compared to polycrystal simulation results.

(*a*) *Tantalum*

Consider a plate of unidirectional rolled body-centred-cubic (BCC) tantalum, from which compression specimen 'blocks' (nominally 5 mm cubes) are cut (as depicted in

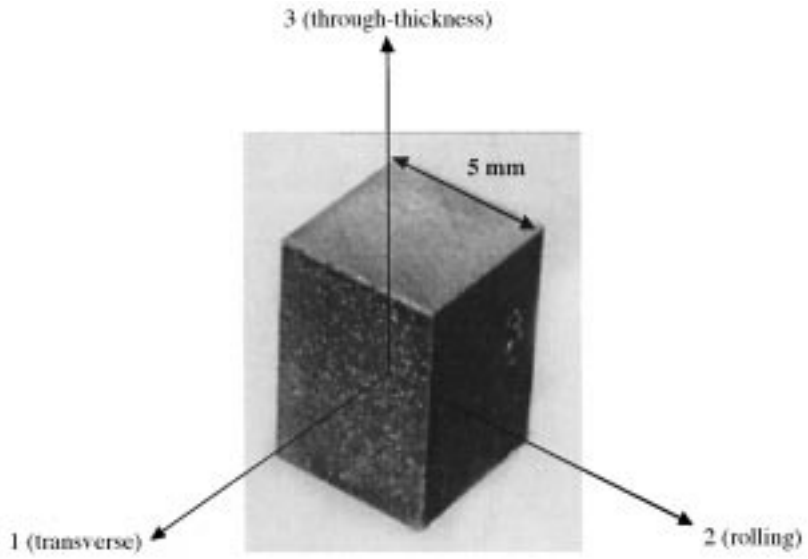

Figure 1. Hexahedral compression test specimen cut from a unidirectional rolled plate of tantalum.

figure 1). These blocks have an associated material coordinate system (basis $\underline{\bar{e}}_i$) as shown in figure 1, where $\underline{\bar{e}}_1$ is transverse to the rolling direction, $\underline{\bar{e}}_2$ corresponds to the rolling direction and $\underline{\bar{e}}_3$ is through-thickness (TT). The manufacturing process for this plate produced a near-orthotropic mild rolling texture, discussed in some detail by Maudlin *et al*. (1998) and Bingert *et al*. (1997).

A set of stress points mapping out a π-plane yield envelope can be generated by repetitive plastic straining probes (polycrystal calculations) of an orientation distribution function (Maudlin *et al*. 1996). For each arbitrary straining direction, a yield stress point is computed via a Bishop–Hill polycrystal calculation using the upper bound option of the LApp (Los Alamos polycrystal plasticity) code (Kocks 1970; Canova *et al*. 1985) with the slip deformation modes $\{110\}\langle 111\rangle$ and $\{112\}\langle 111\rangle$. Such a π-plane yield surface is presented in figure 2, showing a LApp-simulated yield surface, and also a quadratic fit to this LApp piece-wise function; this quadratic function interpolates the LApp results at the horizontal and vertical axis intercepts. The shape coefficients associated with the quadratic fit are given in row 1 of table 1 along with the associated r_{IJ} that are easily computed using equation (2.22).

The blocks of figure 1 were compressed quasi-statically at room temperature in a state of uniaxial stress along each material axis $\underline{\bar{e}}_i$ producing the loading curves presented in figure 3. These curves show that the TT $\underline{\bar{e}}_3$ direction produces the hardest response, with the other in-plane (IP) directions producing *ca.* 20% softer but similar responses. The apparent discontinuities at 4% and 8% strains in these curves represent unload/relubrication/reload steps in the compression testing for the purpose of minimizing surface friction.

Conversion of the uniaxial stress–strain data of figure 3 into $\alpha_{ijkl}\delta_{kl}\delta_{ij}$ (i.e. α_{1122}, α_{1133}, α_{2233}) using equations (2.24) gives the results presented in figure 4. These curves quantify material anisotropy in terms of yield-surface shape coefficients shown as a function of log strain. As confirmed by figure 4, after only 12% strain one would

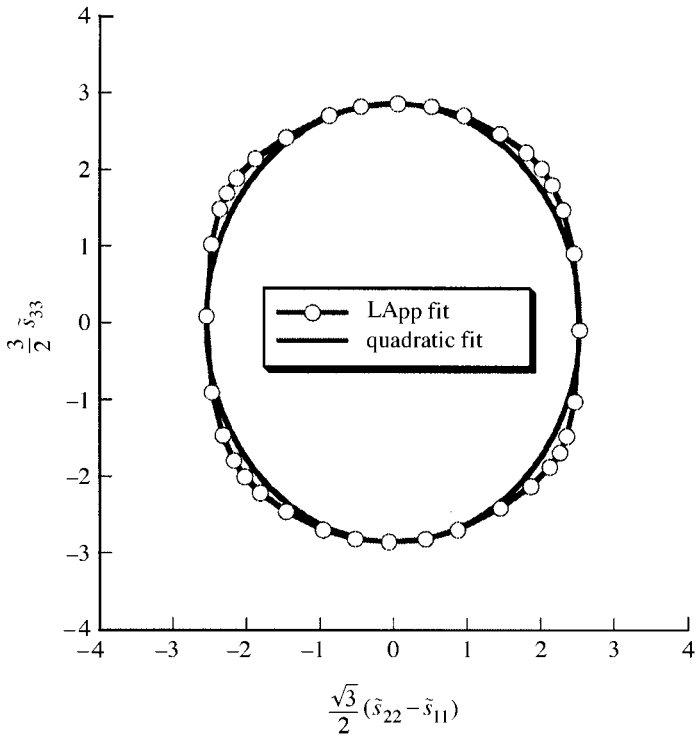

Figure 2. A two-dimensional π-plane subspace showing a polycrystal-generated piece-wise yield surface (line segments and points) being compared with a quadratic fit (solid curve) interpolating the piece-wise function at the horizontal and vertical axis intercepts.

not expect significant texture evolution and, thus, the $\alpha_{ijkl}\delta_{kl}\delta_{ij}$ remain relatively constant. Values for the $\alpha_{ijkl}\delta_{kl}\delta_{ij}$ at 12% strain are given in row 2 of table 1, along with the corresponding r-values as computed using equation (2.22).

(*b*) *Zirconium*

Uniaxial compression testing was conducted on a high-purity crystal-bar zirconium plate, as discussed in detail by Kaschner *et al.* (1998). This hexagonal close-packed metal plate had been clock rolled at room temperature and then annealed at 823 K for 1 h, producing an equiaxed grain structure with a strong in-plane isotropic basal texture (Kaschner *et al.* 1998; Maudlin *et al.* 1998). Next, we associate a material reference frame (basis $\underline{\bar{e}}_i$) with the Zr plate, where the $\underline{\bar{e}}_1 \times \underline{\bar{e}}_2$ plane corresponds to the original rolling plane, and the $\underline{\bar{e}}_3$ direction is TT. Right-circular-cylinder compression samples (nominally 5 mm in diameter by 5 mm in height) were cut from the plate in all three $\underline{\bar{e}}_i$ orientations, i.e. TT ($\underline{\bar{e}}_3$) and IP ($\underline{\bar{e}}_1$ or $\underline{\bar{e}}_2$) specimens. The IP specimens were actually machined at 0°, 45° and 90° relative to the $\underline{\bar{e}}_1$ axis.

Mechanical tests were performed in compression at 76 and 298 K, and at quasi-static strain rates of 0.001 and 0.1 s^{-1} using an Instron screw-drive load frame (Kaschner *et al.* 1998). Figure 5 presents photographs of final geometries for these tests featuring TT and IP ($\underline{\bar{e}}_2$) specimens strained to values of 22% and 30% equivalent plastic strain, respectively.

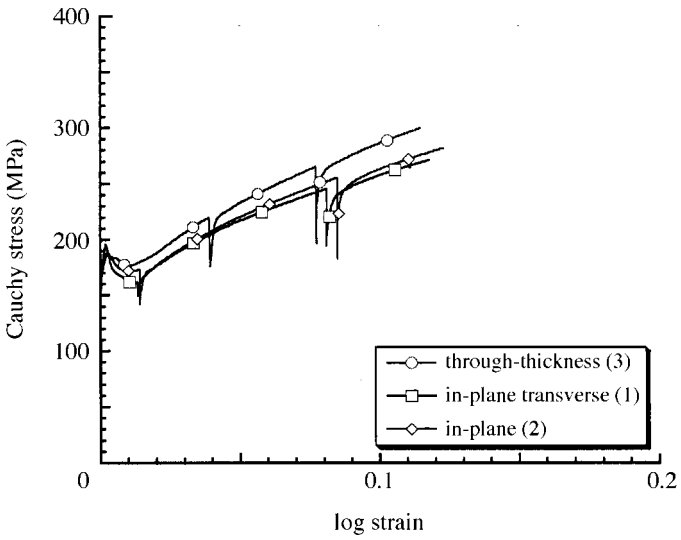

Figure 3. Uniaxial stress–strain curves for a unidirectional rolled Ta plate compressed along each of the material axes $\bar{e}_i$.

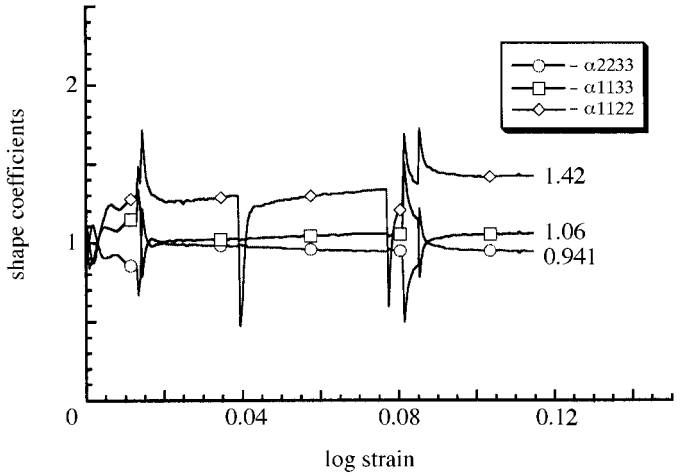

Figure 4. Quadratic shape coefficients evolving as a function of log strain. These coefficients were evaluated using equations (2.24) and the loading curves of figure 3.

A π-plane yield envelope for this Zr material was generated by repetitive plastic straining probes of the texture orientation distribution function given in Maudlin *et al.* (1998). For each arbitrary straining direction, a yield stress point was computed via a self-consistent polycrystal simulation using the code VPSC (Lebensohn & Tomé 1993). Sign-independent prismatic and pyramidal slip deformation modes were assumed in these simulations. The resulting π-plane yield surface is presented in figure 6 presenting a VPSC simulation of a 10% strained shape-hardened yield surface; additional detail is provided in Maudlin *et al.* (1998).

Also shown in figure 6 is a quadratic fit to the polycrystal results, again inter-

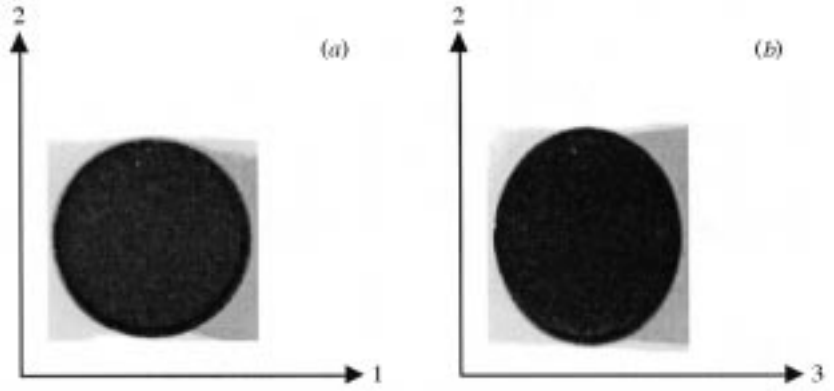

Figure 5. Photographs of the final compression shapes for quasi-static room-temperature uniaxial stress tests for zirconium specimens machined (*a*) through-thickness ($\bar{\underline{e}}_1 \times \bar{\underline{e}}_2$ plane) and (*b*) in-plane ($\bar{\underline{e}}_2 \times \bar{\underline{e}}_3$ plane).

Table 1. *Tantalum r-values and shape coefficients*

experiment or simulation	r_{23}	r_{13}	r_{12}	$-\alpha_{1122}$	$-\alpha_{1133}$	$-\alpha_{2233}$
polycrystal simulations (LApp)	1.25	1.52	1.22	1.37	1.10	0.90
low-rate compression	1.32	1.46	1.10	1.39	1.05	0.95
Taylor cylinder impact (175 m s^{-1})	1.25	1.25	1.00	1.25	1.00	1.00

polating the VPSC piece-wise curve at the horizontal and vertical axis intercepts. This quadratic function misses the stress corners in the VPSC shape, but could be 'accurate enough' depending on the finite-element (FE) application intended for this information. FE simulation of the compression depicted in figure 5 *requires* the use of the piece-wise yield surface to accurately predict the final compression geometries, as discussed in Maudlin *et al*. (1998). A superquadric yield, where the stress components are raised to fractional powers, would better fit the corners apparent in the figure 6 results function (Schiferl & Maudlin 1991). The shape coefficients associated with the quadratic fit are given in row 1 of table 2 along with the corresponding r_{IJ}.

Loading curves for the TT and IP samples are presented in figure 7. The IP compressions produced very similar stress–strain curves along the two IP directions $\bar{\underline{e}}_1$ and $\bar{\underline{e}}_2$, with small variations in stress of *ca.* ± 10 MPa about the mean value for a given set of conditions. This finding supports the expectation of in-plane isotropy for this clock rolled material.

As performed for the tantalum, we converted the uniaxial stress–strain data of figure 7 into $\alpha_{ijkl}\delta_{kl}\delta_{ij}$ using equations (2.24), giving the shape coefficients presented in figure 8. These coefficient curves quantify the very strong plastic anisotropy apparent for this material, and also indicate strong evolution as a function of strain. Specifically, the TT coefficient α_{1122} has a value of 15 (recall that unity corresponds to isotropy) at 10% strain decreasing to about 8 at 22% strain. The other IP coefficients, α_{1133} and α_{2233}, also evolve from their initially rather large values, and symmetrically approach unity at large strain. Values for α_{1122}, α_{1133}, α_{2233} at 22% strain are given in row 2 of table 2 for these quasi-static compression tests, along with the corresponding r-values, as computed using equations (2.22).

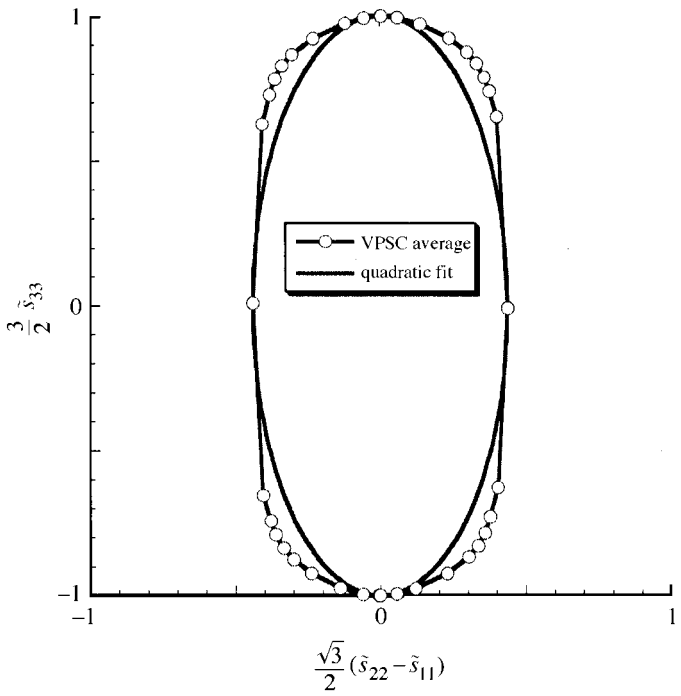

Figure 6. A two-dimensional π-plane subspace showing a piece-wise yield surface (line segments and points) being compared with a quadratic fit (solid curve) interpolating the piece-wise function at the horizontal and vertical axis intercepts.

Table 2. *Zirconium r-values and shape coefficients*

experiment or simulation	r_{23}	r_{13}	r_{12}	$-\alpha_{1122}$	$-\alpha_{1133}$	$-\alpha_{2233}$
polycrystal simulations (VPSC)	7.30	7.30	1.00	7.30	1.00	1.00
low-rate compression	11.16	7.03	0.63	8.65	0.78	1.22
Taylor cylinder impact (243 m s^{-1})	1.42	1.42	1.00	1.42	1.00	1.00

4. High-rate yield-surface comparisons

Taylor test profile data-sets are presented for both tantalum and zirconium metals. Three-dimensional post-impact specimen shapes were digitized in order to estimate the axial distribution of strain. This information is converted into r-values and yield-surface shape coefficients, and is compared with polycrystal simulations.

(*a*) *Tantalum*

Taylor cylinder impact specimens were cut from the same tantalum plate discussed above for the compression blocks. Two IP cylinder orientations (i.e. the cylindrical axes are coincident with either the $\bar{e}_1$ (transverse) or the $\bar{e}_2$ (rolling) material directions) were produced. The Taylor specimens were calibre 30 (7.62 mm diameter) cylinders with a length of 38.1 mm (1.5 in) having the length-to-diameter ratio $L/D = 5$.

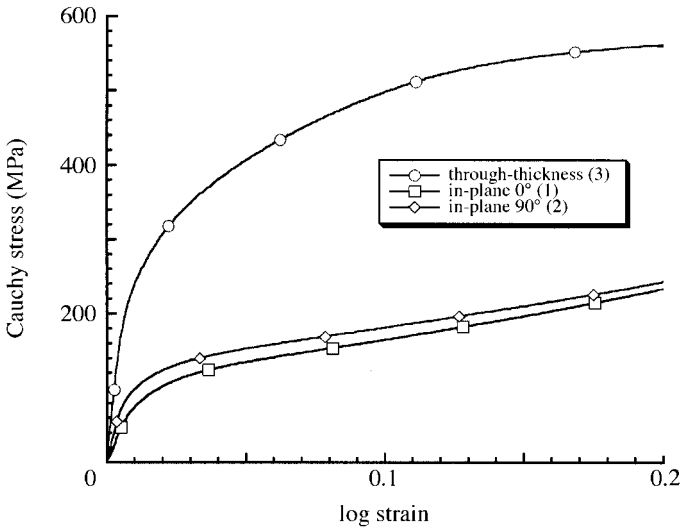

Figure 7. Uniaxial tress–strain curves for a crystal bar clock-rolled Zr material quasi-statically compressed along each of the material axes $\underline{\bar{e}}_i$.

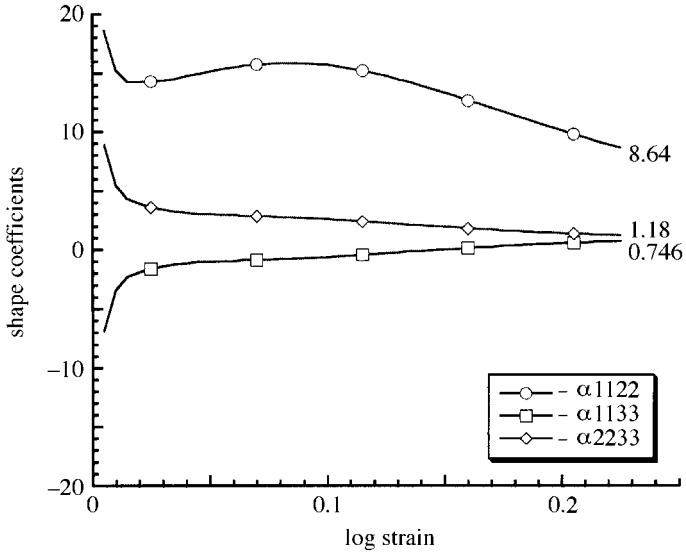

Figure 8. Quadratic shape coefficients evolving as a function of strain. These coefficients were evaluated using equations (2.24) and the loading curves of figure 7.

Taylor tests were conducted at Eglin Air Force Base as described in Maudlin *et al*. (1999), producing three consistent post-test geometries (designated sc-11, sc-12 and sc-21 in Maudlin *et al*. (1999)), all having the general appearance portrayed in figure 9. The cylinders were launched using a calibre 30 Mann powder gun. The velocity of the projectiles was measured using both pressure transducers and parallel laser beams crossing the flight path. Velocities determined from the two systems were *ca*. 175 m s^{-1}, agreeing to within ± 3.0 m s^{-1}. The anvil target was AF1410 steel, heat treated to a surface hardness of Rc 58.

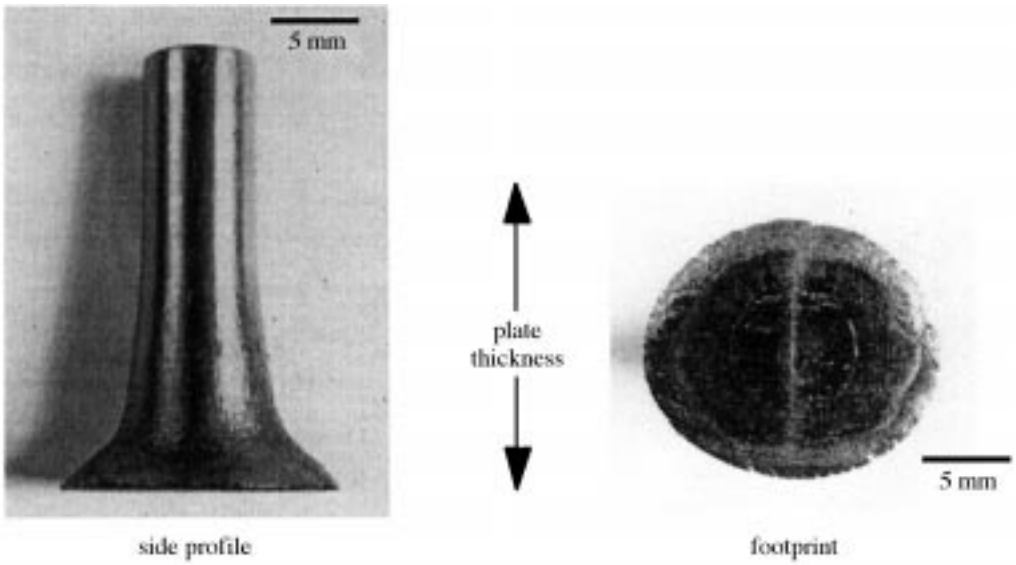

Figure 9. Photographs of the post-test geometry for a tantalum Taylor impact specimen.

After testing, geometric profile data for the deformed specimens were generated using an optical comparator. As discussed in Maudlin *et al.* (1999), the data-set consists of three digitized side profiles for the minor dimension, three digitized side profiles for the major dimension, and three digitized footprints (the cross-sectional area at the impact interface, i.e. the $\bar{\underline{e}}_1 \times \bar{\underline{e}}_3$ or $\bar{\underline{e}}_2 \times \bar{\underline{e}}_3$ plane). All three tests indicated good comparability in terms of the post-test shapes. The digitized footprints, in particular, are nearly identical in shape. Eccentricities (ratio of major to minor diameters) of the footprints range from 1.18 to 1.23 (say an average value of 1.20). Time-integrated r-values are extracted from these footprint geometries using a form similar to equations (2.14) that assumes homogeneous deformation

$$r_{IJ} \cong \int_0^\infty d^{\mathrm{p}}_{II}\,\mathrm{d}t \Big/ \int_0^\infty d^{\mathrm{p}}_{JJ}\,\mathrm{d}t = \frac{\ln(R_I/R_0)}{\ln(R_J/R_0)}, \quad \text{no sum } I, J, \tag{4.1}$$

where R is the specimen radius. Applying equation (4.1) to the Taylor footprint data gives the r-value estimates in row 3 of table 1, along with the inferred shape coefficients. These coefficients were obtained by solving equation (2.24) for the α_{1122}, α_{1133}, α_{2233}, and noting that the resulting set of three linear equations is homogeneous and, thus, does not represent a system of three independent equations; an extra equation is needed to obtain a non-trivial unique solution. This is a consequence of the fact that the yield function given by equation (2.6) has an implied normalization. Assuming that the flow stress σ had been characterized from uniaxial stress data in a specific direction, say in the $\bar{\underline{e}}_I$ direction, then the normalization relationship $-\alpha_{11II} - \alpha_{22II} = 2$ must hold in order to recover a uniaxial stress state from the yield function. This normalization in conjunction with equation (2.24) will produce a unique set of $\alpha_{ijkl}\delta_{kl}\delta_{ij}$.

The use of equation (2.24) to compute $\alpha_{ijkl}\delta_{kl}\delta_{ij}$ from Taylor test r-values assumes that a state of uniaxial stress existed in the specimen during deformation. Based on the FE simulations reported in Jones *et al.* (1992), this is actually a good assumption.

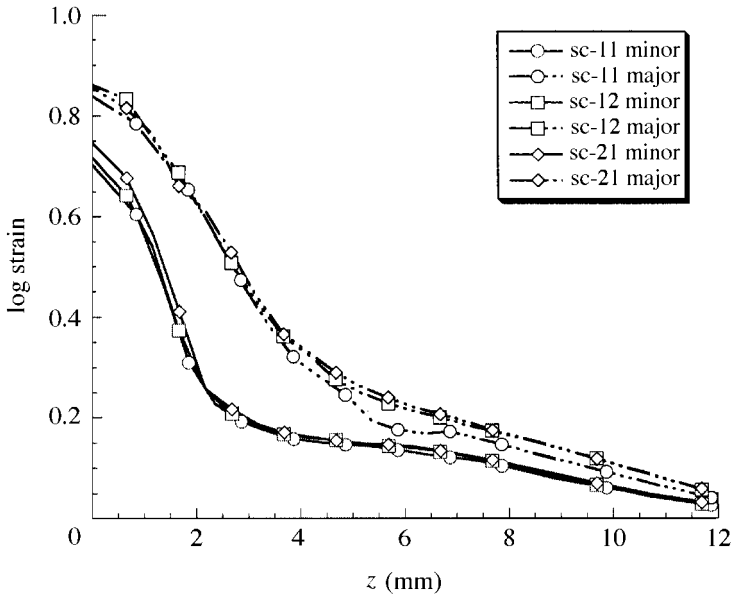

Figure 10. Tantalum Taylor cylinder strain profiles shown as a function of axial position relative to the impact interface. Both major- and minor-side profiles are featured for the various Taylor shots.

Specimen r-values extracted from arbitrary test geometries that do not realize uniaxial stress during deformation require the use of an inverted form of equation (2.31) to compute $\alpha_{ijkl}\delta_{kl}\delta_{ij}$.

Further analysis of the digitized side profiles for these Taylor shots is useful to better understand plastic anisotropy and evolution. Axial strain profiles for both the major and minor sides of the deformed specimens are presented in figure 10. The ordinate is log strain $\ln(R/R_0)$ for the various tests plotted as a function of axial position z, where z is measured relative to the impact interface. The major and minor strains, which are both zero at large z, accumulate at different rates as z decreases. Their maximum values of 87% and 70% are obviously realized at $z = 0$, respectively.

Recasting the figure 10 strain profiles in terms of the r-value (via equation (4.1)) expressed as a function of minor-side strain gives the very interesting results shown in figure 11. Noting the footprint r-values from row 3 of table 1, the r-value from the Taylor specimen profiles actually varies from 1.25 at the impact interface to a peak value of 2.4 at a strain of 20% ($z = 3$ mm), indicating rather strong microstructural evolution as a function of axial position. Note that all three tests depicted in figure 11 are nearly identical from the impact interface down to *ca.* 15% strain, and then diverge at smaller strain (perhaps due to geometric measurement uncertainties). Since r-values are related to yield-surface shape coefficients and shape coefficients reflect the microstructural state of the material, one may conclude from the results of figure 11 that some structural change (possibly in texture, grain shape, etc.) occurs between 15% and 20% strain. At strains greater than 20%, the yield topography evolves rather monotonically back towards the original shape as strains accumulate to 72%.

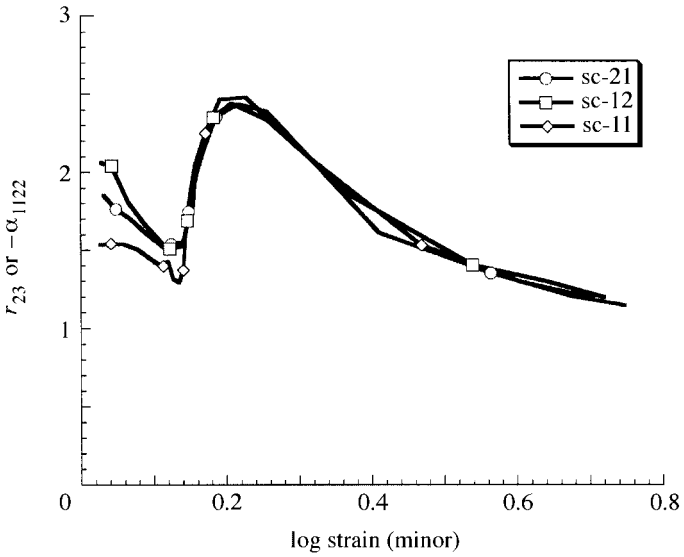

Figure 11. Tantalum Taylor cylinder r-value profiles shown as a function of minor-side log strain for three Taylor shots.

(*b*) *Zirconium*

Taylor cylinder impact specimens were cut from the zirconium plate described above for the cylindrical compression specimens, producing two IP cylinder orientations, i.e. the cylindrical axes are coincident with either the $\bar{e}_1$ or $\bar{e}_2$ plate directions. The Taylor specimens were calibre 30 (7.62 mm diameter) cylinders with a length of 2 in (50.8 mm) having an L/D ratio of 6.67.

Taylor tests were conducted at Los Alamos National Laboratory at various velocities: 50, 101, 170 and 243 m s^{-1}. The 243 m s^{-1} Taylor shot is portrayed in figure 12 in terms of major- and minor-side profiles and the impact footprint. These cylinders were launched using a calibre 30 He-gas-driven gun. The velocity of the projectiles was measured using parallel laser beams crossing the flight path. The anvil target was AF1410 steel, heat treated to a surface hardness of Rc 58 and lapped to a mirror finish.

Post-test geometric profile data for the 243 m s^{-1} specimen were generated using interface reconstruction software from the National Institute of Health (NIH). The input data-set for the NIH software consisted of high-resolution electronic scans of the photographed side profiles for the major and minor dimensions and a footprint. The reconstructed footprint showed an eccentricity of 1.10. Approximate r-values extracted from the footprint geometry of figure 12 (using equation (4.1) and the procedure discussed above for the tantalum tests) are given in row 3 of table 2, along with the inferred shape coefficients. Row comparison of table 2 indicates large differences in shape coefficients between the high- and low-rate testing.

Further analysis of the digitized side profiles for the zirconium Taylor shot was conducted in an analogous fashion to that discussed in § 4 *a*. Axial strain profiles for both the major and minor sides of the deformed specimens as inferred from the NIH results are presented in figure 13. The ordinate is log strain plotted as a function of axial position z, where z is measured relative to the impact interface. The major

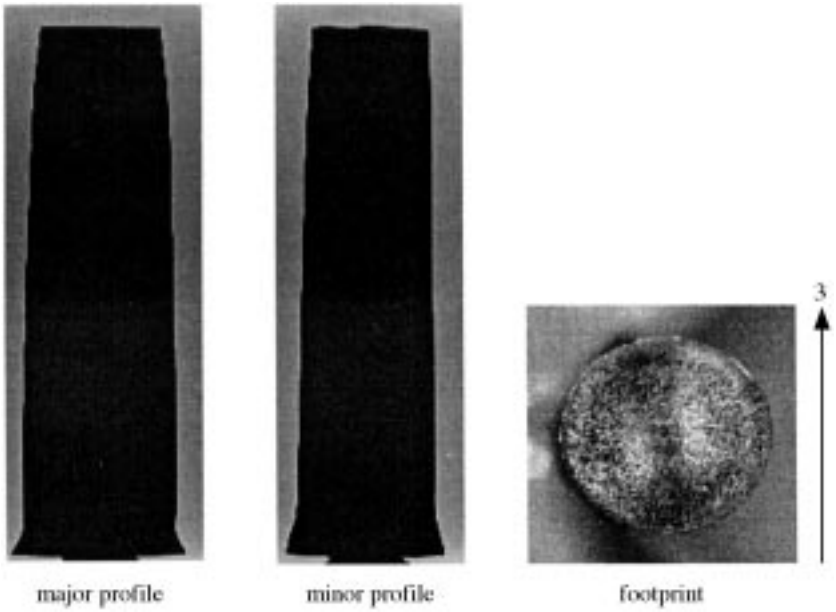

Figure 12. Photographs of the post-test geometry for a zirconium Taylor specimen.

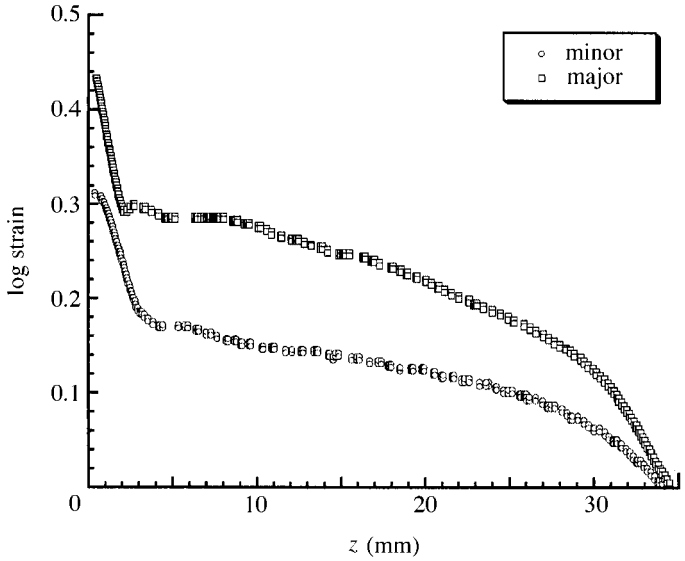

Figure 13. Zirconium Taylor cylinder strain profiles shown as a function of axial position relative to the impact interface. Strains for both the major and minor dimensions are shown.

and minor strains, which are both zero at large z, accumulate at different rates as z decreases; their maximum values of 44% and 31%, respectively, are obviously realized at $z = 0$.

Recasting via equation (4.1), the figure 13 strain profiles in terms of r-values expressed as a function of minor-side strain give the interesting result shown in figure 14. The footprint r-value of 1.42 (from row 3 of table 2) is seen to decrease to

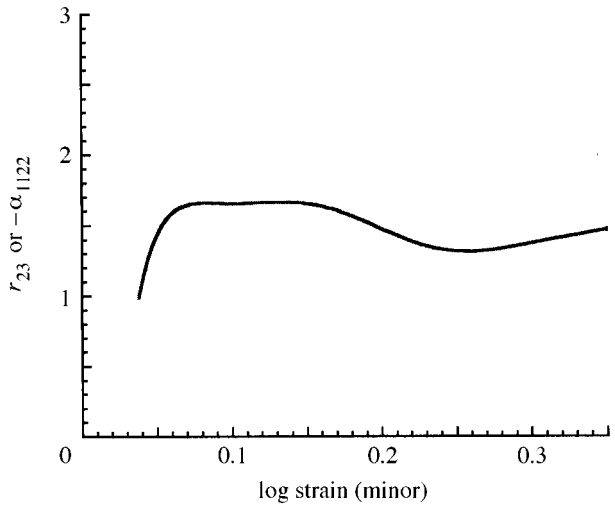

Figure 14. Zirconium Taylor cylinder r-value profile shown as a function of minor-side log strain.

1.3 in figure 14, and it then increases to a plateau value of 1.65 at 15% strain. As strain goes to zero, the r-value drops precipitously to unity. The evolution of anisotropy portrayed by figure 14 is quite mild compared to the dramatic quasi-static results of figure 8.

5. Discussion of results

Review of tables 1 and 2 indicates variability in the values for the Ta and Zr quadratic shape coefficients, but the important question from an applications point of view is how significant are these differences. Figure 15 illustrates the table 1 shape coefficients as π-plane ellipses using equation (2.6). It is obvious from this figure that all of the methodologies for estimating yield topography that are discussed above, i.e. rate-independent polycrystal simulations, low strain-rate compression testing (10^{-3} s^{-1}), and high-strain-rate Taylor testing (greater than 10^4 s^{-1}), all predict nearly the same yield-surface shape. Therefore, for Ta, and possibly for other BCC materials where two modes of slip deformation represent a good assumption, the use in FE calculations of a rate-independent yield-surface shape is well justified.

In like manner, figure 16 illustrates the table 2 zirconium quadratic coefficients as π-plane ellipses. Again note that the low-strain-rate compression testing and rate-independent polycrystal simulations both produce very similar ellipses in the π-plane. However, the high-strain-rate Taylor testing predicts yield topography that is dramatically less anisotropic, demonstrating an interesting rate effect. Obviously, the rather limited deformation mechanisms (prismatic and pyramidal slip) present in the lower-symmetry Zr at quasi-static rates must transition somehow at higher rates. This high-rate behaviour must introduce additional deformation mechanisms (other competing slip and twinning modes) in such a way that the Taylor loading is accommodated with much less directional deformation. Initial metallographic examination of Zr deformed at high rate reveals evidence of substantial twin activation,

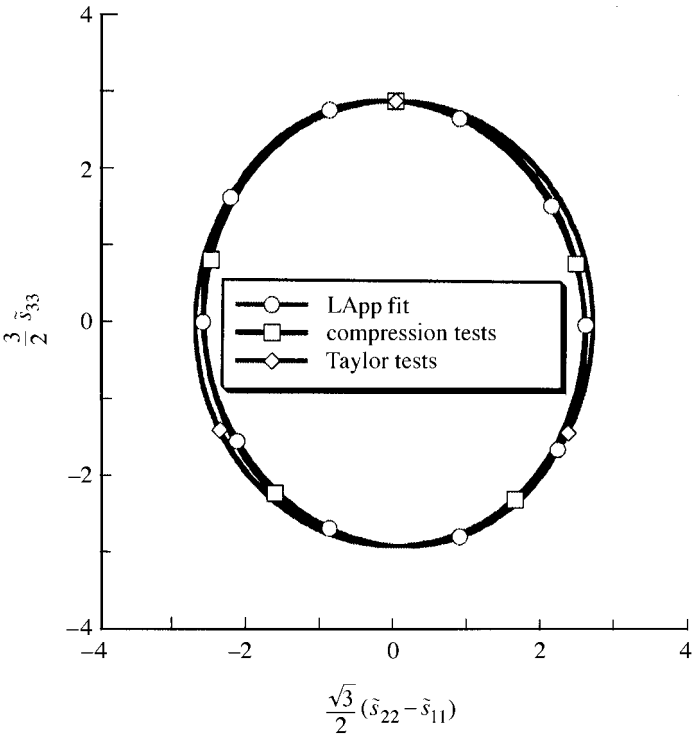

Figure 15. A π-plane subspace comparison of quadratic tantalum yield functions as interpolated from LApp simulations and experimentally extracted in terms of r-values from the quasi-static compression tests and Taylor cylinder impact tests.

which is consistent with this postulate. High-rate FE code constitutive modelling involving a lower-symmetry material like Zr needs to be cognizant of this behaviour.

The effect of evolution on yield-surface shape can be judged for Ta and Zr after review of both the low-rate and high-rate experimental data-sets. In the proceeding discussion, it is difficult to unfold from the experimental information whether the evidence of shape coefficient evolution with respect to strain is related to grain reorientation, grain-shape changes or some transition of the dominant deformation mechanisms. For Ta, the low-rate results of figure 4 show virtually constant shape coefficients (ignoring the unload/reload transients) out to the rather modest strain of 12%. It would be interesting to extend the experimental loading for these compression blocks to larger strain. The high-rate Taylor results of figure 11, which extend to 80% strain, show moderate shape coefficient evolution: the coefficient α_{1122} jumps from 1.4 to 2.5, and then decreases slowly back to approximately 1.25 during the course of the Taylor impact event. This high-rate evolution in yield topography implies concurrent texture and grain-shape evolution, and possibly some slip mode competition. However, the practical side of the importance of this topography evolution is that the strain-averaged shape of figure 11 is very close to the initial shape, and, thus, the importance of evolution for Ta is seen to vanish for the integrated Taylor test. For Zr, the low-rate figure 8 results show strong yield topography evolution and, thus, strong implied deformation mechanism transition and texture evolution; the coef-

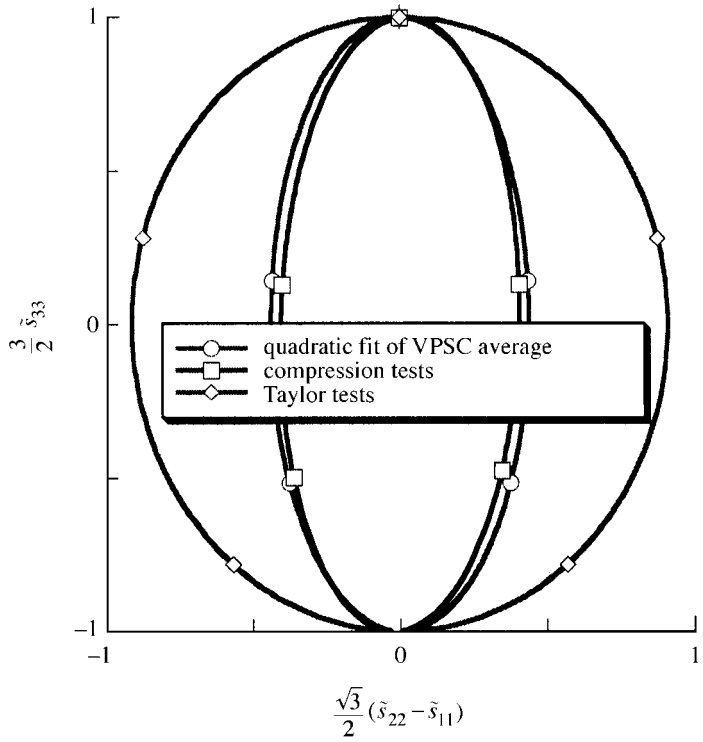

Figure 16. A π-plane subspace comparison of quadratic zirconium yield functions as interpolated from VPSC simulations and experimentally extracted in terms of r-values from the quasi-static compression tests and Taylor cylinder impact tests.

ficient α_{1122} evolves from 18 to 8.6 as the compression specimen realizes only 30% strain. The high-rate analysis of the Zr Taylor test specimen in terms of the figure 14 r-value versus strain results shows much less anisotropy and even less evolution. This implies that texture and grain-shape evolution, and possible slip mode competition, have only a minor impact on yield-surface topography at these high rates.

The authors acknowledge the efforts of C. P. Trujillo and T. M. Bell for the design and operation of the Los Alamos Taylor Anvil test facility, and the efforts of A. J. Honey in the digitization of the zirconium Taylor cylinder profiles. This work was performed under the auspices of the US Department of Energy.

References

Bingert, J. F., Desch, P. B., Bingert, S. R., Maudlin, P. J. & Tomé, C. N. 1997 Texture evolution in upset-forged P/M and wrought tantalum: experimentation and modeling. In *Proc. 4th Int. Conf. Tungsten Refractory Metals and Alloys: Processing, Properties, and Applications*, pp. 169–178. Metal Powder Industries Federation, Princeton, NJ, USA.

Canova, G. R., Kocks, U. F., Tomé, C. N. & Jonas, J. J. 1985 The yield surface of textured polycrystals. *J. Mech. Phys. Solids* **33**, 371–397.

Chen, S. R. & Gray III, G. T. 1996 Constitutive behavior of tantalum and tantalum–tungsten alloys. *Metall. Trans.* A **27**, 2994–3006.

Follansbee, P. S. & Kocks, U. F. 1988 A constitutive description of the deformation of copper based on the use of mechanical threshold stress as an internal state variable. *Acta Metall.* **36**, 81–93.

Hawkyard, J. B. 1969 A theory for the mushrooming of flat-ended projectiles impinging on a flat rigid anvil, using energy considerations. *Int. J. Mech. Sci.* **11**, 313.

Hill, R. 1950 *The mathematical theory of plasticity*. Oxford University Press.

Jones, S. E., Maudlin, P. J., Gillis, P. P. & Foster Jr, J. C. 1992 An analytical interpretation of high strain rate material behavior during early time plastic deformation in the Taylor impact test. In *Proc. Computers in Engineering 1992* (ed. G. A. Gabriele), vol. 2, p. 173. New York: ASME.

Kaschner, G. C., Gray III, G. T. & Chen, S. R. 1998 Influence of texture and impurities on the mechanical behavior of zirconium. In *Shock Compression of Condensed Matter 1997* (ed. S. C. Schmidt, D. P. Dandekar & J. W. Forbes), pp. 435–438. Woodbury, NY: American Institute of Physics.

Kocks, U. F. 1970 The relation between polycrystal deformation and single crystal deformation. *Metall. Trans.* **1**, 1121–1143.

Lebensohn, R. A. & Tomé, C. N. 1993 A self-consistent anisotropic approach for the simulation of plastic deformation and texture development of polycrystals. Application to zirconium alloys. *Acta Metall. Mater.* **41**, 2611–2624.

Lee, E. H. & Tupper, S. J. 1954 Analysis of plastic deformation in a steel cylinder striking a rigid target. *J. Appl Mech.* **21**, 63.

Maudlin, P. J. & Schiferl, S. K. 1996 Computational anisotropic plasticity for high-rate forming applications. *Comp. Meth. Appl. Mech. Engng* **131**, 1–30.

Maudlin, P. J., Wright, S. I. & Gray III, G. T. 1995 Application of facetted yield surfaces for simulating uniaxial stress compression tests of textured materials. In *Proc. EXPLOMET 95 Conf., El Paso, TX, August 1995*. New York: Marcel Dekker.

Maudlin, P. J., Wright, S. I., Kocks, U. F. & Sahota, M. S. 1996 An application of multisurface plasticity theory: yield surfaces of textured materials. *Acta Metall. Mater.* **44**, 4027–4032.

Maudlin, P. J., Foster Jr, J. C. & Jones, S. E. 1997 On the Taylor test. Part III. A continuum mechanics code analysis of steady plastic wave propagation. *Int. J. Impact Engng* **19**, 231–256.

Maudlin, P. J., Tomé, C. N., Kaschner, G. C. & Gray III, G. T. 1998 Introduction of polycrystal constitutive laws in a finite element code with applications to zirconium forming. In *Simulation of materials processing: theory, methods and applications* (ed. J. Huetink & F. P. T. Baaijens). Rotterdam: A. A. Balkema.

Maudlin, P. J., Bingert, J. F., House, J. W. & Chen, S. R. 1999 On the modeling of the Taylor cylinder impact test for orthotropic textured materials: experiments and simulations. *Int. J. Plasticity* **15**, 139–166.

Noble, B. 1969 *Applied linear algebra*. Englewood Cliffs, NJ: Prentice-Hall.

Schiferl, S. K. & Maudlin, P. J. 1991 Texture-induced anisotropy and high-strain-rate deformation in metals. In *Shock waves and high-strain-rate phenomena in materials* (ed. M. A. Meyers, L. E. Murr & K. P. Staudhammer). New York: Dekker.

Taylor, G. I. 1948 The use of flat-ended projectiles for determining dynamic yield stress. I. Theoretical considerations. *Proc. R. Soc. Lond.* A **194**, 289.

Wilson, L. L., House, J. W. & Nixon, M. E. 1989 Time resolved deformation from the cylinder impact test. US Air Force Report AFATL-TR-89-76, Eglin Air Force Base.

PHILOSOPHICAL TRANSACTIONS OF THE ROYAL SOCIETY A MATHEMATICAL, PHYSICAL & ENGINEERING SCIENCES